Theoretical and Applied Fracture Mechanics 119 (2022) 103380

Contents lists available at ScienceDirect

Theoretical and Applied Fracture Mechanics

journal homepage: www.elsevier.com/locate/tafmec

Defect induced cracking and modeling of fatigue strength for an additively manufactured Ti-6Al-4V alloy in very high cycle fatigue regime

Weiqian Chi [a], Wenjing Wang [a,*], Ying Li [b], Wei Xu [b], Chengqi Sun [c,d,*]

[a] Key Laboratory of Vehicle Advanced Manufacturing, Measuring and Control Technology (Beijing Jiaotong University), Ministry of Education, Beijing 100044, China
[b] Aviation Key Laboratory of Science and Technology on Aeronautical Materials Testing and Evaluation, Beijing Key Laboratory of Aeronautical Materials Testing and Evaluation, Beijing Institute of Aeronautical Materials, Beijing 100095, China
[c] State Key Laboratory of Nonlinear Mechanics, Institute of Mechanics, Chinese Academy of Sciences, Beijing 100190, China
[d] School of Engineering Science, University of Chinese Academy of Sciences, Beijing 100049, China

ARTICLE INFO

Keywords:
Very high cycle fatigue
Additively manufactured titanium alloy
Defect
Fatigue strength modeling

ABSTRACT

Additively manufactured (AM) alloy usually inevitably contains defects during the manufacturing process or in service. Defect, as a harmful factor, could significantly reduce the fatigue performance of materials. This paper shows that the location and introduced form of defects play an important role in high cycle fatigue and very high cycle fatigue (VHCF) behavior of selective laser melting Ti-6Al-4V alloys. The S-N curve descends approximately linearly for internal defect induced failure. While for artificial surface defect induced failure, the S-N curve descends at first and then exhibits a plateau region feature. The competition of interior crack initiation with fine granular area feature is also observed in VHCF regime. The paper indicates that only the size or the stress intensity factor range of the defect is not an appropriate parameter for describing the effect of defect on fatigue crack initiation. Finally, the effect of artificial surface defect on high cycle fatigue and VHCF strength is modeled, i.e., the fatigue strength σ, fatigue life N and defect size $\sqrt{area}$ (square root of the projection area of defect perpendicular to principal stress direction) is expressed as $\sigma = \begin{cases} C N^a (\sqrt{area})^n, & N < N_0 \\ C N_0^a (\sqrt{area})^n, & N \geq N_0 \end{cases}$, where C, a and n are constants, and N_0 is the number of cycles at the knee point of the curve.

1. Introduction

Additive manufacturing, with its manufacturing flexibility, offers possibility to fabricate customized prototypes with complicated geometries in a rapid design to manufacturing cycle [1–3]. As an essential member, additively manufactured (AM) titanium alloys have potentially wide use in aviation, aerospace, biomedical and nuclear industries [4–6]. Some components are inevitably subjected to high cycle fatigue and very high cycle fatigue (VHCF) loadings in service [7]. Researchers in recent years have found that the failure of metallic materials (e.g. steels, Ti-alloys, magnesium alloys) could still occur in VHCF regime [8–11], so as for the AM Ti-alloys [12–14]. The fracture surface of AM Ti-6Al-4V alloy presents the fish eye pattern and fine granular area (FGA) feature for the interior crack initiation in VHCF regime [13–17]. FGA is a typical characteristic on the fracture surface for VHCF failure. The equivalent crack growth rate in FGA is below one lattice spacing ($\sim 10^{-10}$ m) per cycle [18,19] and the stress intensity factor range of FGA approaches to the threshold value of crack propagation for high strength steels [20–22].

Moreover, the as-built Ti-alloys generally contain AM defects during the manufacturing process (e.g. gas porosity or lack of fusion) [23–26]. This type of defect tends to induce fatigue crack initiation and significantly lowers the fatigue performance of AM Ti-alloys [15,16,27–30]. It has been shown that the hot-isostatic pressing (HIP) could effectively eliminate or reduce the manufacturing defects and the fatigue performance of AM Ti-alloys after HIP could be comparable to the conventionally processed wrought materials [14,31–33]. However, due to the size limitation of HIP equipment, HIP is impractical for the big structures such as aircraft engine components by now. Consequently, the fatigue behavior of AM alloys with manufacturing defects needs to be further

* Corresponding authors at: Key Laboratory of Vehicle Advanced Manufacturing, Measuring and Control Technology (Beijing Jiaotong University), Ministry of Education, Beijing 100044, China (W. Wang). State Key Laboratory of Nonlinear Mechanics, Institute of Mechanics, Chinese Academy of Sciences, Beijing 100190, China (C. Sun).
E-mail addresses: wjwang@bjtu.edu.cn (W. Wang), scq@lnm.imech.ac.cn (C. Sun).

https://doi.org/10.1016/j.tafmec.2022.103380
Received 19 March 2022; Received in revised form 22 April 2022; Accepted 27 April 2022
Available online 2 May 2022

Table 1
Mechanical properties of the non-HIP and HIP AM Ti-6Al-4V alloy.

Type of material	Tensile stress (MPa)	Yield stress (MPa)
Non-HIP	1007	951
HIP	946	849

elucidated. Beside the manufacturing defects of the material, the defects such as impact holes, corrosion pits or scratches might as well exist in engineering component surface during service and degrade the fatigue performance [34,35]. Therefore, it is essential to fully understand the influence of different types of defects on the fatigue behavior of AM Ti-alloys in order to meet the demand of high reliability of components.

Motivated by the above considerations, the defect induced high cycle fatigue and VHCF behavior is investigated for an AM Ti-6Al-4V alloy by selective laser melting in this paper. The effect of artificial surface defect and manufacturing defect are both considered. The crack initiation mechanism at different kinds of defects is analyzed by scanning electron microscope (SEM) observation. The competition between the artificial surface defect induced cracking and the interior AM defect induced cracking is further discussed in view of the defect size and stress intensity factor range for the defect. Finally, the effect of artificial surface defect on high cycle and VHCF strength is modeled based on the concept of $\sqrt{area}$ parameter. The model is also used to predict the effect of surface defect on the fatigue strength of the EA4T steel in literature.

2. Materials and methods

2.1. Materials

The AM Ti-6Al-4V alloy used in this paper is manufactured by selective laser melting technique on a BLT-S310 machine. The chemical composition (wt.%) of the powder is 5.97 Al, 3.93 V, 0.12 Fe, 0.088 O, 0.015 C, 0.0031 H and Ti balance. At first, two batches of bars with a length of 100 mm and a diameter of 12 mm are manufactured. The building direction is vertical. Then, they are heat-treated at 710 °C for 2 h in vacuum and cooled in argon atmosphere. One batch of bars is post-processed by HIP at 920 °C and 1000 bar for 2 h in argon atmosphere to reduce the porosity and defect. The other batch of bars is without HIP process (i.e., non-HIP). The values of the tensile strength and yield strength are listed in Table 1, which are obtained from three specimens with the gauge length of 30 mm and diameter of 5 mm. Fig. 1a and 1b show the microstructure parallel to the building direction for the non-HIP and HIP AM Ti-6Al-4V alloy, respectively. The microstructure is basketweave with lamellar α phase. The thickness of the lamellar by HIP is generally bigger than that without the HIP process.

2.2. Fatigue test and characterization

For the HIP AM Ti-6Al-4V alloy, smooth specimens and specimens with three kinds of artificial surface defects (i.e., defect-A, defect-B and defect-C) are considered in order to investigate the effect of defect size on the fatigue behavior. For the non-HIP AM Ti-6Al-4V alloy, smooth specimens and specimens with artificial surface defect-A are considered

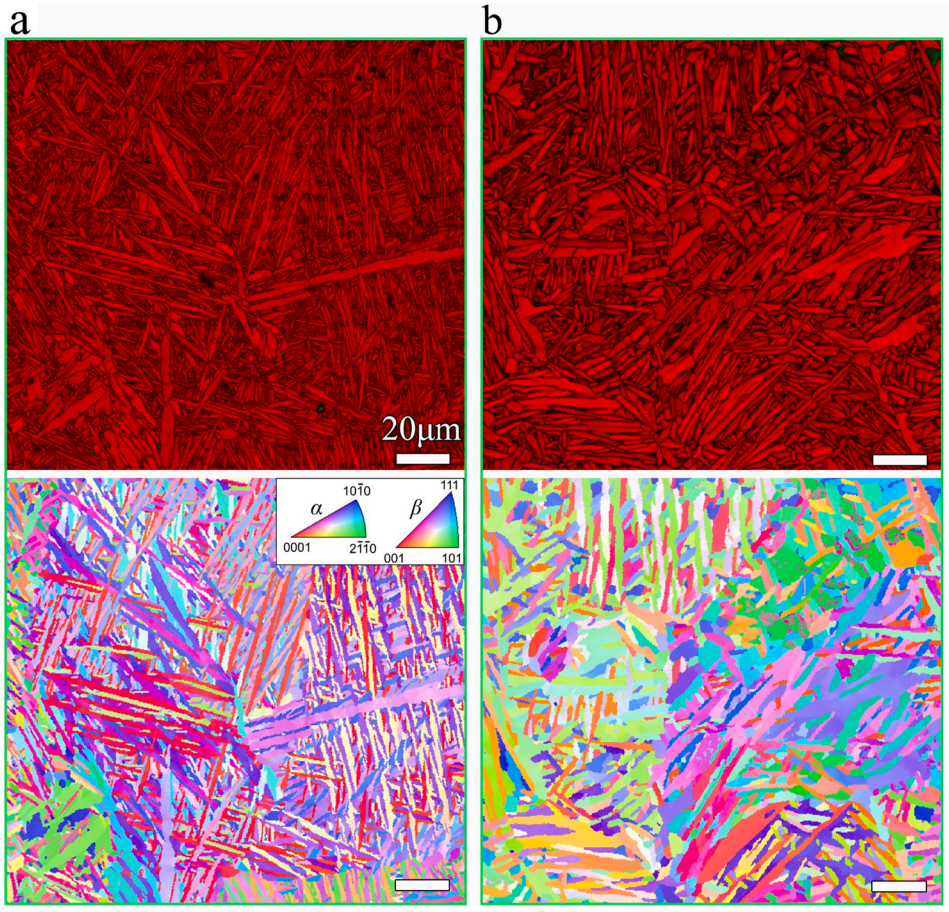

Fig. 1. (a) and (b): Microstructure of non-HIP and HIP AM Ti-6Al-4V alloy, respectively. The top panel is an image quality map with phase distribution (α phase: red, β phase: green), and the bottom panel is an inverse pole figure. The scale bars in (a) and (b) are all 20 μm. (For interpretation of the references to colour in this figure legend, the reader is referred to the web version of this article.)

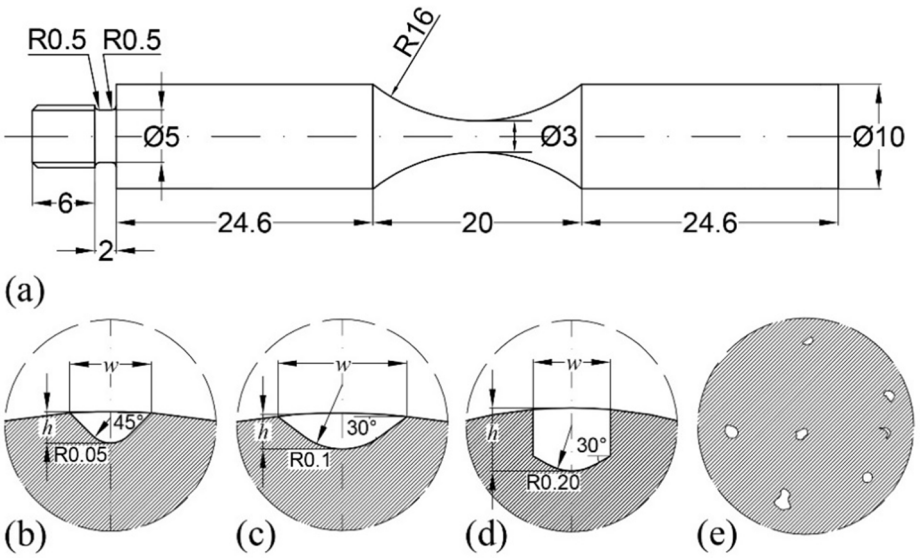

Fig. 2. Sketch maps of specimen and defect. (a): Fatigue specimen (in mm); (b)-(d) Cross section of defect-A, defect-B and defect-C perpendicular to the specimen axis. (e) AM defect of the material.

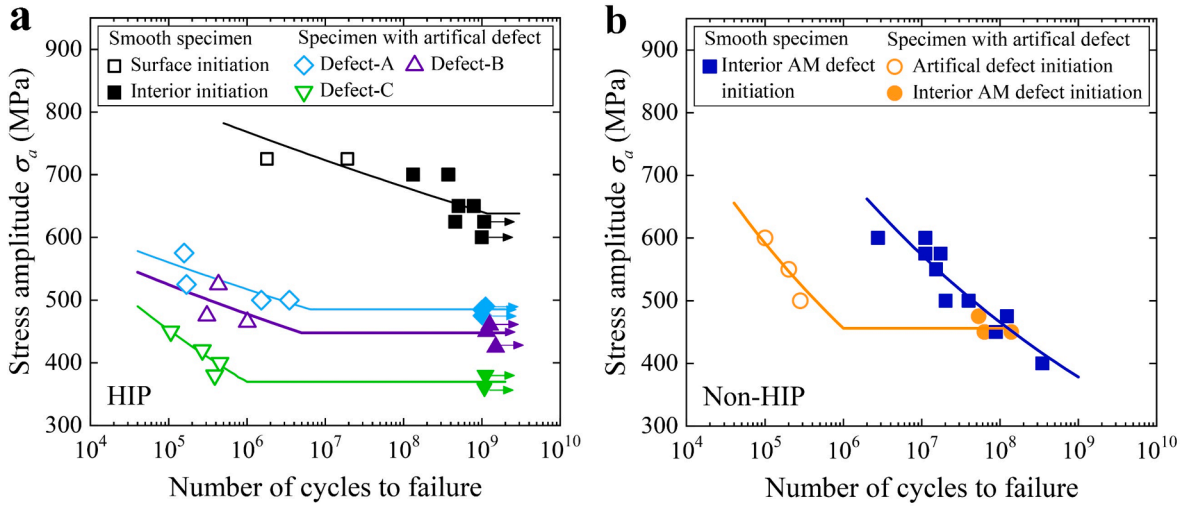

Fig. 3. S-N data of HIP and non-HIP specimens with and without artificial surface defect, in which the lines are fitted by the bilinear relation of the S-N data in log–log scale [39]. (a): HIP specimens with and without artificial surface defect, in which the arrows denote that the specimens do not fail at the associated fatigue cycles; (b): non-HIP specimens with and without artificial surface defect.

in order to investigate the effect of different types of defects. Some of the results for non-HIP smooth specimens are also available in Ref. [17]. The artificial surface defects are drilled at the smallest section of the specimen with different bit diameters, similar to that in Ref. [36]. The geometry of the smooth specimen is shown in Fig. 2a. The approximate shape and geometry of the artificial defects are shown in Fig. 2b-2d based on the observation of the fatigue fracture surface of the specimen failed from the surface defect. The size of defects and the values of w and h are measured by Image-Pro Plus (IPP) software on SEM images of the fracture surface. The sketch map of the AM defect of the material is given in Fig. 2e for comparison. Before fatigue test, the surfaces of the hourglass part of smooth specimens and specimens with artificial surface defect (before the defect is drilled) are ground and polished.

The fatigue tests are all conducted in air and at room temperature with an ultrasonic fatigue testing system (USF-2000A, $f = 20$ kHz). An adjustable spot cooling system is employed to reduce the temperature of the specimen during fatigue test. The machine is controlled by a piezoelectric converter, and the supplied voltage is equivalent to a certain output displacement amplitude. The fatigue loading is controlled by the output displacement of the device. The output voltage with the displacement amplitude of the standard sample is calibrated with an eddy current extensometer. The applied stress amplitude at the smallest section of the specimen is at first transformed to the displacement by the theoretical formula [37]. The stress ratio R is -1, and the fatigue loading without intermittence is used.

The fracture surface morphologies of failed specimens are observed by SEM. The microstructure is observed by SEM at 20 kV using an electron backscatter diffraction detector and analyzed in the OIM Analysis software.

3. Experimental results and analyses

3.1. S-N data of smooth specimens and specimens with artificial surface defect

Fig. 3 shows the S-N data of smooth specimens and specimens with

Table 2
Stress amplitude σ_a, fatigue life N, defect size a_{def} at the crack origin, and the width w and depth h of the artificial surface defect at the crack origin for non-HIP specimens.

Smooth specimens			Specimens with artificial surface defect-A				
σ_a (MPa)	N	a_{def} (μm)	σ_a (MPa)	N	a_{def} (μm)	w (μm)	h (μm)
600	1.12×10^7	77	600*	1.00×10^5	102	184	72
600	2.76×10^6	56	550*	2.01×10^5	101	201	64
575	1.74×10^7	49	500*	2.82×10^5	107	243	69
575	1.12×10^7	53	475	5.33×10^7	41	–	–
550	1.53×10^7	74	450	6.40×10^7	49	–	–
500	2.02×10^7	68	450	1.39×10^8	57	–	–
500	3.99×10^7	43	450	6.29×10^7	54	–	–
475	1.23×10^8	50					
450	8.86×10^7	44					
400	3.49×10^8	77					

* It denotes that the specimen fail from artificial surface defect.

Table 3
Stress amplitude σ_a, and fatigue life N for HIP smooth specimens.

σ_a (MPa)	N	σ_a (MPa)	N
725	1.80×10^6	650	5.05×10^8
725	1.91×10^7	625	4.58×10^8
700	3.73×10^8	625*	1.07×10^9
700	1.32×10^8	600*	1.00×10^9
650	7.89×10^8		

* It denotes that the specimen does not fail at the tested fatigue cycles.

artificial surface defect for both non-HIP and HIP specimens, in which the stress amplitude is calculated by the smallest section of the specimen disregarding the drilled hole for the specimens with artificial surface defect. The detailed information of the stress amplitude, fatigue life and the defect at the crack origin are shown in Table 2-4, respectively. In this paper, the crack origin denotes the main crack origin unless it is noted otherwise. The defect size is taken as the square root of the defect projection area perpendicular to the principal stress and a smooth enclosing contour line is considered for the AM defect with irregular shape [38]. It is observed from Fig. 3 that the S-N data exhibit two patterns for different types of defect induced fatigue failure. It has the plateau region feature for both the HIP specimens and non-HIP specimens with artificial surface defect. However, for the internal AM defect induced fatigue failure, the fatigue strength decreases with increasing the fatigue life. Furthermore, there is a critical value of the stress level for the artificial surface defect induced failure. When the stress amplitude is higher than the critical value, the crack initiates from artificial surface defect, and the fatigue strength decreases approximately linearly with increasing the fatigue life. Once the stress amplitude is lower than the critical one, the artificial surface defect does not influence the fatigue behavior, as shown in Fig. 3b. This indicates that the location and introduced form of defect play a vital role in the fatigue behavior of AM Ti-6Al-4V alloy. Fig. 3a also shows that the fatigue strength of HIP specimens is decreased with the increase of artificial surface defect size.

In addition, Fig. 3 indicates that the HIP AM Ti-6Al-4V alloy shows a better fatigue property than the non-HIP AM Ti-6Al-4V alloy in VHCF regime. For example, the fatigue strength at 10^9 cycles is 378 MPa for non-HIP smooth specimens and 638 MPa for HIP smooth specimens

Table 4
Stress amplitude σ_a, fatigue life N, defect size a_{def}, defect width w and defect depth h at the crack origin for HIP specimens with artificial surface defect-A, defect-B and defect-C, respectively.

Specimen type	σ_a (MPa)	N	a_{def} (μm)	w (μm)	h (μm)
Specimen with defect-A	575	1.57×10^5	84	182	67
	525	1.69×10^5	91	171	74
	500	3.49×10^6	82	201	59
	500	1.52×10^6	86	175	67
	490*	1.12×10^9	–	–	–
	485*	1.00×10^9	–	–	–
	475*	1.01×10^9	–	–	–
Specimen with defect-B	525	4.34×10^5	132	365	82
	475	3.08×10^5	167	415	108
	465	1.01×10^6	122	339	81
	460*	1.26×10^9	–	–	–
	450*	1.15×10^9	–	–	–
	425*	1.51×10^9	–	–	–
Specimen with defect-C	450	1.06×10^5	223	324	165
	420	2.69×10^5	244	317	202
	400	4.53×10^5	234	327	186
	380	3.88×10^5	231	322	176
	380*	1.10×10^9	–	–	–
	360*	1.08×10^9	–	–	–

* It denotes that the specimen does not fail at the tested fatigue cycles.

from the fitting line. The fatigue strength of specimens after HIP is about 69% higher compared with the non-HIP specimens. Moreover, the fatigue strength at 10^9 cycles is 448 MPa for the HIP specimen with

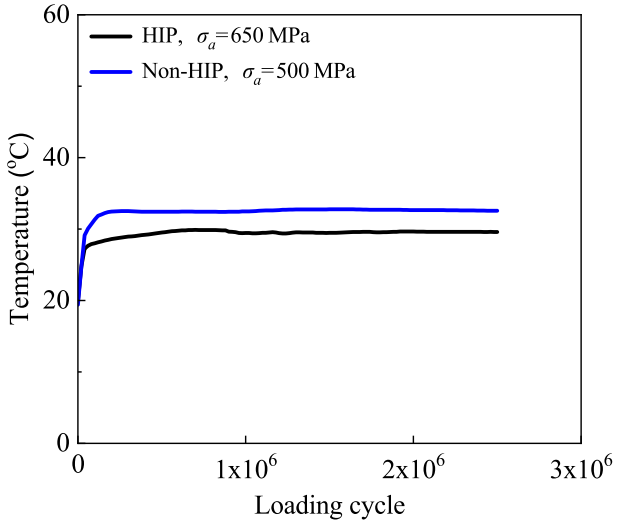

Fig. 4. Variation of surface temperature of specimens with loading cycle during ultrasonic frequency fatigue test.

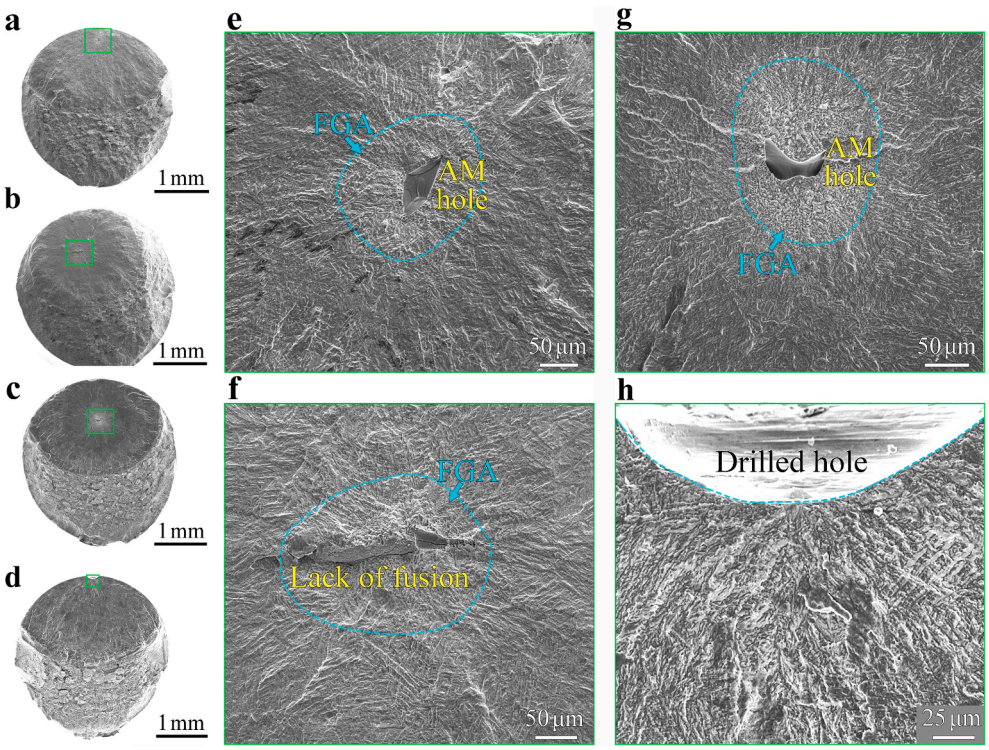

Fig. 5. Fatigue fracture surface morphology of non-HIP specimens. (a) and (e): smooth specimen, $\sigma_a = 600$ MPa, $N = 2.76 \times 10^6$; (b) and (f): smooth specimen, $\sigma_a = 550$ MPa, $N = 1.53 \times 10^7$; (c) and (g): specimen with artificial surface defect, $\sigma_a = 450$ MPa, $N = 1.39 \times 10^8$; (d) and (h): specimen with artificial surface defect, $\sigma_a = 500$ MPa, $N = 2.82 \times 10^5$. (a)-(d): the whole morphology of fatigue fracture surface; (e)-(h): close-ups of the rectangular regions in (a)-(d), respectively.

artificial surface defect-B from the fitting line. It is higher than the fatigue strength (378 MPa) at 10^9 cycles for the non-HIP specimen with artificial surface defect due to the effect of AM defect in the material itself. By the consideration that the fatigue strength at 10^9 cycles decreases with increasing the artificial surface defect size (Fig. 3a) and the size of defect-B for the HIP specimen is bigger than that of the artificial surface defect for the non-HIP specimen, the HIP technique improves significantly the VHCF strength of the AM Ti-6Al-4V alloy with small artificial surface defect at 10^9 cycles.

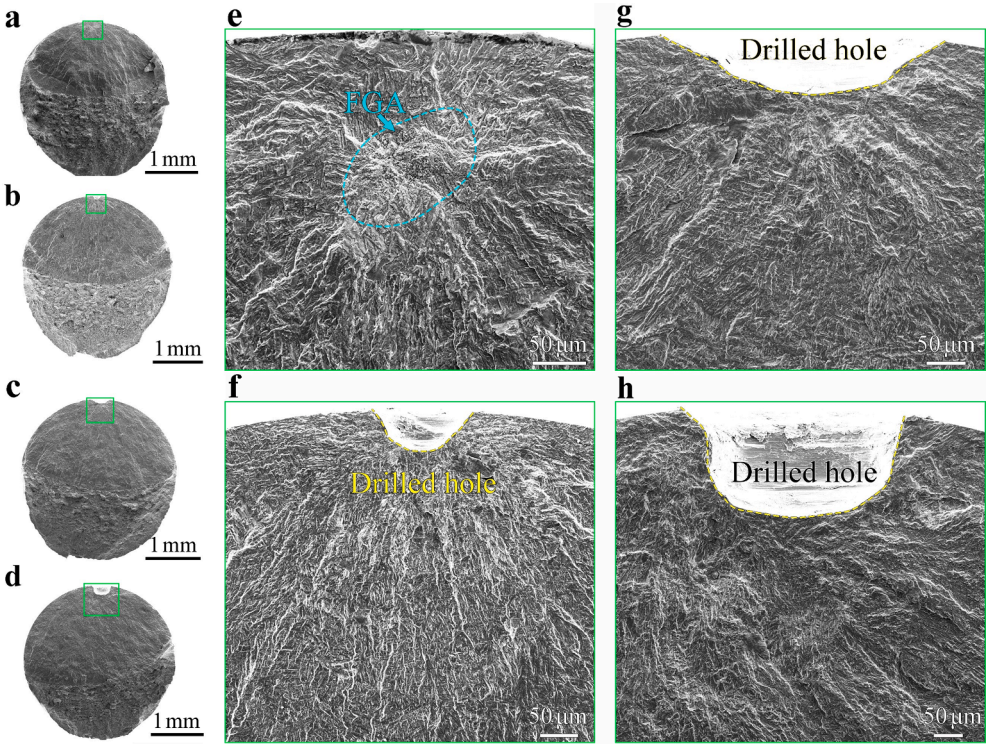

Fig. 6. Fatigue fracture surface morphology of HIP specimens. (a) and (e): smooth specimen, $\sigma_a = 700$ MPa, $N = 1.32 \times 10^8$; (b) and (f): specimen with artificial surface defect, $\sigma_a = 525$ MPa, $N = 1.69 \times 10^5$; (c) and (g): specimen with artificial surface defect, $\sigma_a = 525$ MPa, $N = 4.34 \times 10^5$; (d) and (h): specimen with artificial surface defect, $\sigma_a = 420$ MPa, $N = 2.69 \times 10^5$. (a)-(d): the whole morphology of fatigue fracture surface; (e)-(h): close-ups of the rectangular regions in (a)-(d), respectively.

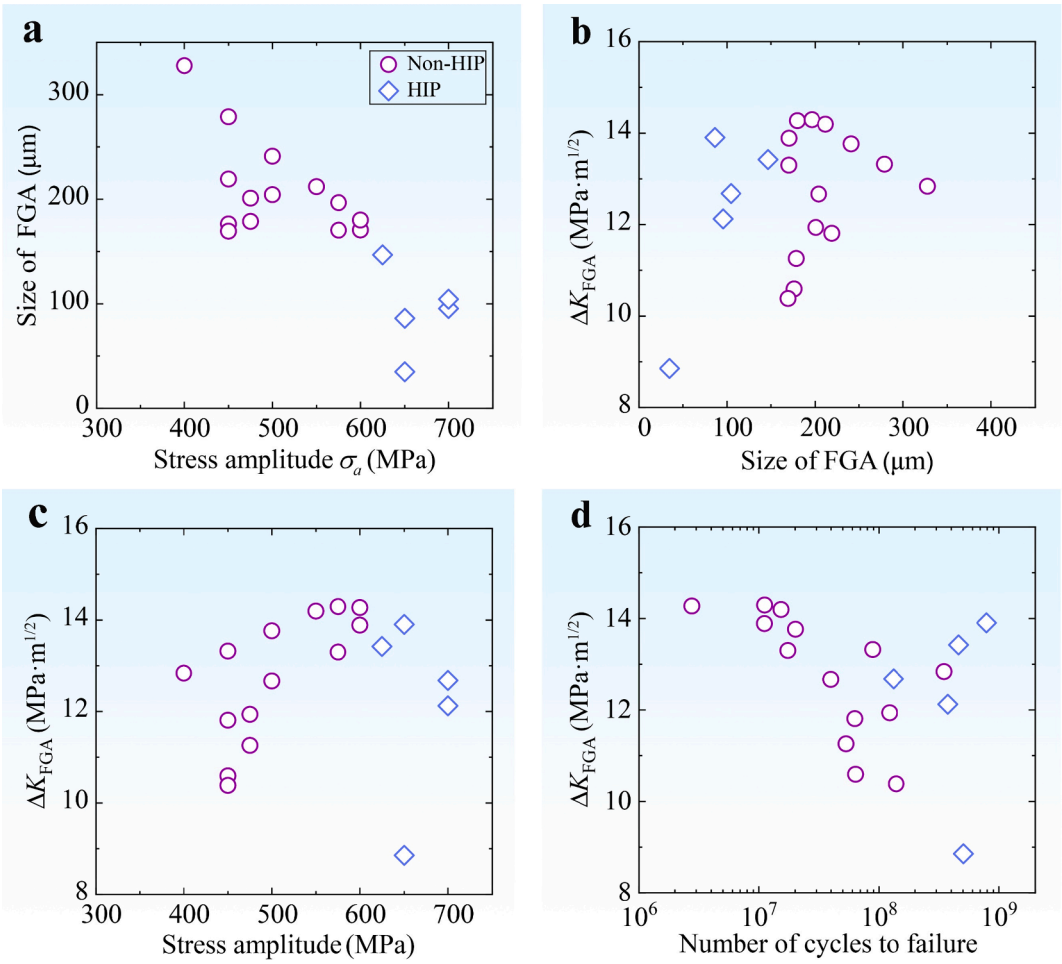

Fig. 7. (a): FGA size versus stress amplitude for interior crack initiation; (b)-(d): ΔK_{FGA} versus FGA size, stress amplitude and fatigue life for interior crack initiation, respectively.

3.2. Temperature measurement of specimens

The surface temperature of the smallest section is measured by a thermocouple (k-type) for both the HIP and non-HIP specimens during the ultrasonic frequency fatigue test, as that used in literature [17]. Fig. 4 shows the variation of the surface temperature with the loading cycle at the stress amplitude $\sigma_a = 650$ MPa for the HIP specimen and at the stress amplitude $\sigma_a = 500$ MPa for the non-HIP specimen. It is seen that the stable temperature is not very high (about 30 °C). This indicates that the temperature is near to the room temperature for both the HIP and non-HIP specimens tested in VHCF regime.

3.3. Fracture surface morphology

3.3.1. Non-HIP AM Ti-6Al-4V alloy

For smooth specimens, the fatigue crack initiates from the internal hole (Fig. 5e) except one specimen fails at the lack of fusion (Fig. 5f). However, the crack initiation site is related to the stress level for the specimen with artificial surface defect. At the higher stress amplitude, the crack initiates from the artificial surface defect (Fig. 5h). While at the lower stress amplitude, the crack initiates from the internal AM defect (Fig. 5g), similar to that of the smooth specimen. In this case, the artificial surface defect does not affect the crack initiation for the non-HIP AM Ti-6Al-4V alloy, and the fatigue fracture surface exhibits the fish eye pattern with FGA feature similar to that observed for the AM Ti-alloys in VHCF regime [14–16].

3.3.2. HIP AM Ti-6Al-4V alloy

Unlike the non-HIP smooth specimens that failed from the internal AM defect, the fatigue crack initiates from the microstructure inhomogeneity (e.g. bigger α-phase or cluster of α-phase) for all the HIP smooth specimens [14,15]. The crack initiation and early growth region also presents the FGA morphology, as shown in Fig. 6e. For HIP specimens with artificial surface defect, the fatigue crack initiates from the drilled hole, as shown in Fig. 6f-6h.

3.4. Stress intensity factor range for FGA

It has been indicated that the FGA consumes most of the fatigue life for VHCF of high strength steels [18,19] and Ti-alloys [17,40] and that the stress intensity factor range of FGA approaches the threshold value of crack propagation [20–22]. Here, the stress intensity factor range of FGA is also calculated similar to that used in literature [38], i.e., $\Delta K_{FGA} = 0.5\Delta\sigma\sqrt{\pi a_{FGA}}$ ($\Delta K_{FGA} = 0.65\Delta\sigma\sqrt{\pi a_{FGA}}$ for the FGA near to the specimen surface), in which a_{FGA} is square root of the fine granular area including the defect area on the fracture surface.

Fig. 7a gives the relation between FGA size and the stress amplitude for both HIP and non-HIP specimens. It is seen that the FGA size tends to decrease with increasing the stress amplitude. The variation of ΔK_{FGA} on FGA size, stress amplitude and fatigue life is plotted in Fig. 7b-7d, respectively. The value of ΔK_{FGA} ranges from 10.4 to 14.2 MPa·m$^{1/2}$ for non-HIP specimens, which is close to the range of 8.8 to 14.0 MPa·m$^{1/2}$ of the value of ΔK_{FGA} for HIP specimens.

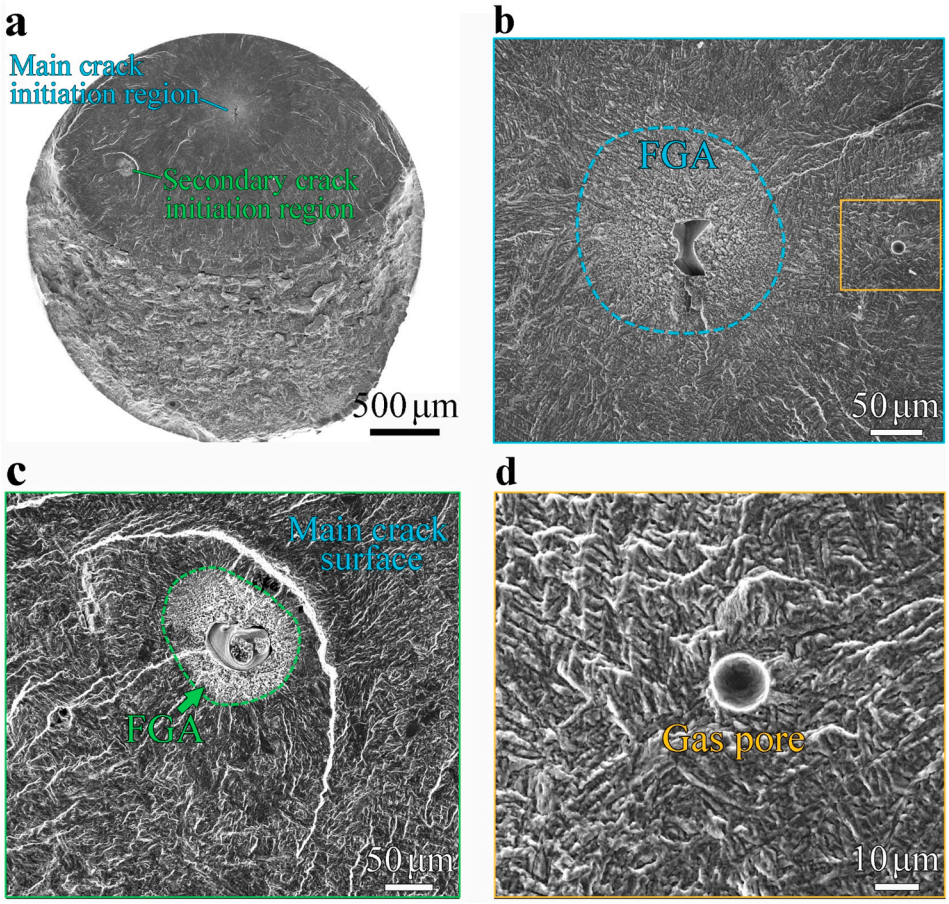

Fig. 8. SEM image of multiple crack initiation for the specimen failed at $\sigma_a = 450$ MPa and $N = 6.40 \times 10^7$ cycles. (a): the whole fatigue fracture surface morphology; (b): enlarged image for the main crack initiation region with FGA morphology; (c): enlarged image of the secondary crack initiation region with FGA morphology; (d): enlarged image for a gas pore without inducing crack initiation at the fracture surface in (b).

4. Discussion

4.1. Competition of crack initiation site

The multiple internal AM defect induced crack initiation with FGA morphology is observed for one of the specimens with artificial surface defect, as shown in Fig. 8a-8c. The AM defect (i.e., gas pore) without inducing crack initiation is also observed on the fracture surface (Fig. 8b and 8d). Here, the sizes of defect in crack origin and defect without inducing crack initiation in Fig. 8 are measured and analyzed by the consideration that the larger defect usually leads to a lower fatigue life or fatigue strength [22,38,41]. The size of defect is 49 μm for the main crack origin and is 55 μm for the secondary crack origin. They are both bigger than the size (11 μm) of the defect without inducing crack initiation. The defect that induces the main crack has a smaller size than the defect that induces the secondary crack, but the FGA size for the main crack is bigger. This indicates that the crack initiation and early growth depend not only on the defect size but also on the microstructure of the material around the defect. Further, all the three AM defect sizes are significantly smaller than the artificial surface defect size (bigger than 100 μm based on the results in Table 2) at the non-HIP specimen. Nevertheless, the internal AM defect induces the fatigue failure of the specimen. It indicates that the introduced form of the defect plays a vital role in the crack initiation and fatigue failure.

In Sec. 3.3.1, it shows that the crack initiation site is related to the stress level. For a further analysis, Fig. 9a shows the variation of defect size at the crack origin with the stress amplitude for the non-HIP specimens with and without artificial surface defect. It is seen that there is a critical value of the stress amplitude. When the stress level is lower than the critical value, the fatigue crack initiates from the internal AM defect even if the artificial surface defect size is bigger than the internal AM defect size, namely that only the defect size could not explain well the influence of defect type on the fatigue crack initiation.

The stress intensity factor range of the defect at the crack origin is also compared between the non-HIP smooth specimen and the non-HIP specimen with artificial surface defect. The stress intensity factor range for the internal AM defect (i.e., ΔK_{int}) and the artificial surface defect (i.e., ΔK_{art}) at the crack origin are calculated by $\Delta K_{int} = 0.5\Delta\sigma\sqrt{\pi a_{int}}$ and $\Delta K_{art} = 0.65\Delta\sigma\sqrt{\pi a_{art}}$ [38], respectively, in which a_{int} and a_{art} denote the internal AM defect size and the artificial surface defect size at the crack origin, respectively. Fig. 9b shows the variation of ΔK_{int} and ΔK_{art} with the stress amplitude. It is seen that the fatigue crack initiates from the internal AM defect though the stress intensity factor range for the artificial surface defect is bigger than that for the internal AM defect at the crack origin when the stress level is below the critical value. This indicates that only the stress intensity factor range of the defect is also not an appropriate parameter for describing the effect of defect on the fatigue crack initiation. In fact, the residual stress, roughness and microstructure at the defect usually differ for different types of defects, which will affect the crack initiation [42–47]. Hence, for the effect of defect on fatigue crack initiation, it needs to consider the influence of the comprehensive factors, such as the stress level, defect size, location of the defect, microstructure around the defect, residual stress and roughness at the defect, etc.

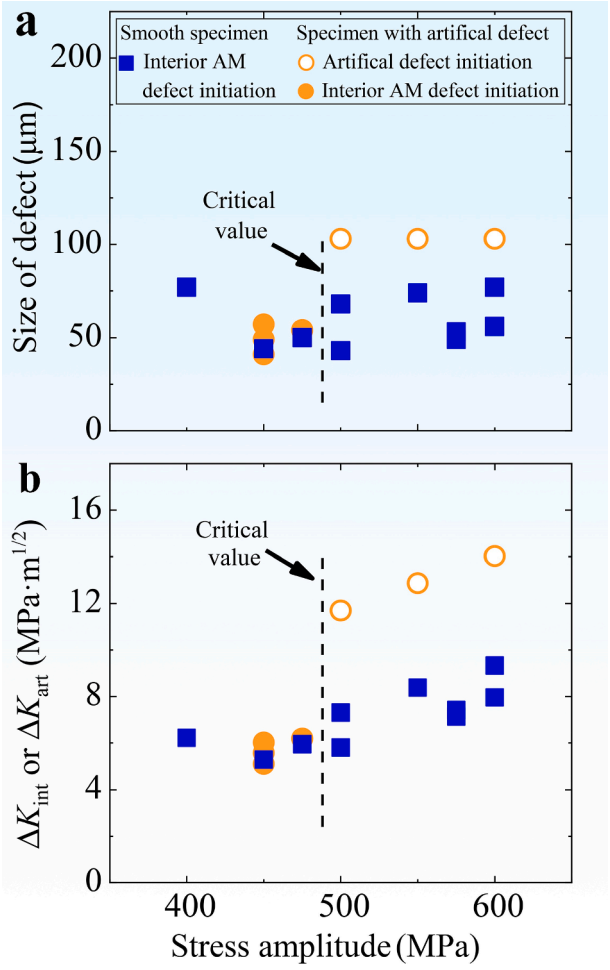

Fig. 9. Size and stress intensity factor range of the defect at the crack origin versus stress amplitude for non-HIP specimens with and without artificial surface defect, in which the average defect size is used for the artificial surface defect. (a): defect size at crack origin versus stress amplitude; (b): ΔK_{int} for the internal AM defect or ΔK_{art} for the artificial surface defect at the crack origin versus stress amplitude.

4.2. Fatigue strength model incorporating defect

The results on non-HIP smooth specimens and the specimens with artificial surface defect show that the effect of defect on fatigue performance is related to the introduced form of the defect. This is also indicated by the high cycle fatigue of S38C steel with different types of defects [46]. Here, the effect of the same type of defect (i.e., the artificial surface defect) on the fatigue strength is investigated. Some models have been proposed for correlating the influence of defect on fatigue strength [48,49]. For example, Murakami and Endo [50] proposed that the fatigue limit of metallic materials incorporating the effect of surface defect could be expressed as $\sigma_w = 1.43(H_V+120)/(\sqrt{area})^{1/6}$, in which H_V (kgf/mm^2) denotes the hardness and $\sqrt{area}$ (μm) denotes the square root of the projection area of defect perpendicular to the principal stress direction. The $\sqrt{area}$ model has been developed to investigate the effect of defect on the fatigue strength of metallic materials [36,41,51–54]. By the consideration that the S-N curve for the specimens with artificial surface defect descends at first and then exhibits a plateau region feature, the bilinear model for the S-N curve [39,55] is developed for describing the high cycle fatigue and VHCF strength incorporating the effect of defect, i.e.,

$$\sigma = \begin{cases} C N^a (\sqrt{area})^n, & N < N_0 \\ C N_0^a (\sqrt{area})^n, & N \geq N_0 \end{cases} \tag{1}$$

where C, a and n are constants, N_0 is the number of cycles at the knee point of the curve.

Eq. (1) can be written as.

$$\log_{10}\sigma = \begin{cases} a(\log_{10}N - \log_{10}N_0) + B, & N < N_0 \\ B, & N \geq N_0 \end{cases} \tag{2}$$

where $B = \log_{10}C + a\log_{10}N_0 + n\log_{10}\sqrt{area}$.

For determination of parameters, the values of a, B and N_0 are at first obtained from the experimental data of specimens with one kind of defect size by iterative calculation to minimize the value of the following equation [39]:

$$\sum_{N_k<N_0} [\log_{10}\sigma_k - a\log_{10}(N_k/N_0) - B]^2 + \sum_{N_k \geq N_0} (\log_{10}\sigma_k - B)^2 \tag{3}$$

where σ_k is fatigue strength, N_k is the associated fatigue life, $k = 1, 2, \ldots, m$, and m is the number of specimens for analysis.

Then, the parameter n in Eq. (1) is determined from the following

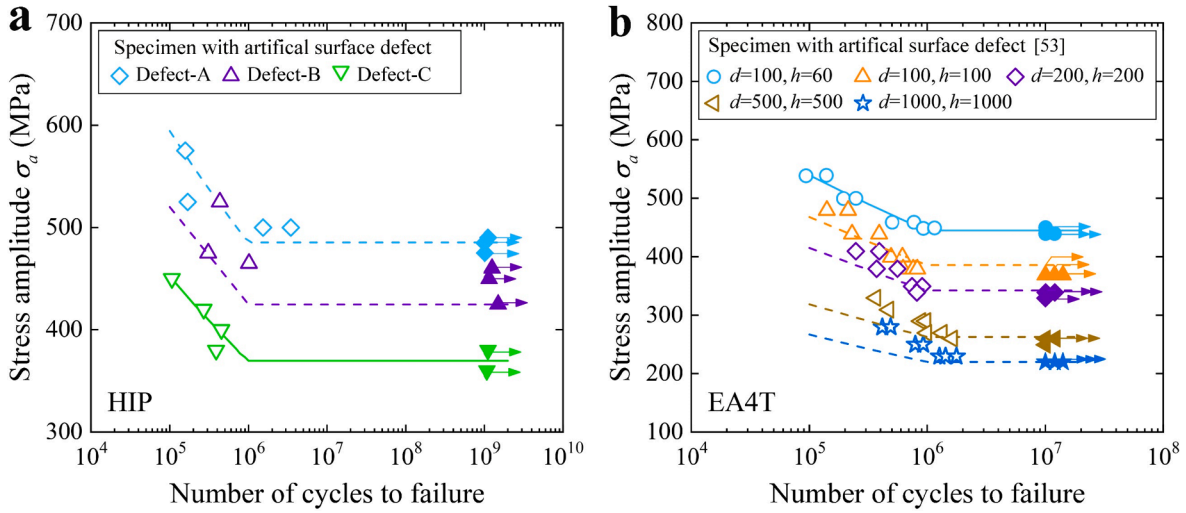

Fig. 10. Comparison of the present model with experimental data. (a): present HIP specimens; (b): micro-shot peened EA4T steel in literature [53]. The solid lines are fitted by the bilinear relation of the S-N data in log–log scale [39]; the dash lines are the predicted results by the present model Eq. (1).

equation by employing the fatigue strength of specimens with another kind of defect size at a certain fatigue life (e.g. 10^7 cycles):

$$\frac{\sigma'}{\sigma''} = \frac{(\sqrt{area'})^n}{(\sqrt{area''})^n} \tag{4}$$

where σ' denotes the fatigue strength of specimens with one kind of defect size $\sqrt{area'}$, and σ'' denotes the fatigue strength of specimens with another kind of defect size $\sqrt{area''}$.

Fig. 10a shows the present model for correlating the fatigue strength of HIP specimens with different sizes of artificial surface defect. Here, the average defect size in Table 4 is used by the consideration that the difference of defect size is very small for the same type of defect. The values of a, B and N_0 are at first obtained from the specimen with defect-C, and then the parameter n is determined by employing the fatigue strength (at 10^7 cycles) of the specimen with defect-A. The fatigue strength is obtained from the fitting line shown in Fig. 3. Fig. 10a shows that the present model Eq. (1) gives a good correlation for the effect of artificial surface defect on the high cycle fatigue and VHCF strength of the AM Ti-6Al-4V alloy. For a further validation of the present model with experimental data, it is used to predict the effect of artificial surface defect on the EA4T steel in literature [53]. The result is shown in Fig. 10b. The values of a, B and N_0 are at first obtained from the specimen with the defect of $d = 100$ μm and $h = 60$ μm, and then the parameter n is determined by the fatigue strength of the specimen with the defect of $d = 1000$ μm and $h = 1000$ μm. The fatigue strength is obtained from the fitting line by the bilinear relation of the S-N data in log–log scale [39]. Fig. 10b indicates that the predicted S-N curves are generally in agreement with experimental data for the effect of defect. This indicates that the present model is promising for correlating the effect of surface defect on the high cycle fatigue and VHCF strength of metallic materials. It is noted that there is a critical size for defect, smaller than which the defect has no influence on the fatigue strength [36,42]. In this case, the model is not applicable. It is also noted that the model might not be valid when the defect size is very large [46].

5. Conclusions

In this paper, the defect induced high cycle fatigue and VHCF behavior of an AM Ti-6Al-4V alloy is studied by using ultrasonic frequency fatigue test. Based on experimental results and analyses, the main conclusions of this study are as follows:

(1) The effect of defect on high cycle fatigue and VHCF behavior of the AM Ti-6Al-4V alloy is related to the location and the introduced form of the defect. For the internal AM defect induced failure, the fatigue life increases with decreasing the stress amplitude. While for the artificial surface defect induced failure, the S-N curve descends at first and then exhibits a plateau region feature.

(2) The fatigue failure caused by the internal defect presents fish eye pattern and FGA morphology in VHCF regime for both the non-HIP and HIP specimens of the AM Ti-6Al-4V alloy. The value of ΔK_{FGA} varies in the range of 10.4–14.2 MPa·m$^{1/2}$ for non-HIP specimens and 8.8–14.0 MPa·m$^{1/2}$ for HIP specimens. Competition of interior crack initiation with FGA feature is also observed in VHCF regime. The paper indicates that only the defect size or stress intensity factor range for the defect cannot correlate well the effect of defect on the fatigue life or fatigue crack initiation position.

(3) A model is proposed for correlating the effect of artificial surface defect on high cycle fatigue and VHCF strength, i.e., the fatigue strength σ, fatigue life N and defect size $\sqrt{area}$ is expressed as $\sigma = \begin{cases} CN^a(\sqrt{area})^n, & N < N_0 \\ CN_0^a(\sqrt{area})^n, & N \geq N_0 \end{cases}$, where C, a and n are constants, N_0 is the number of cycles at the knee point of the curve. The model reflects the plateau region feature of the S-N data for the artificial surface defect induced fatigue failure, and it is in agreement with the experimental data of the present AM Ti-6Al-4V alloy and the data of the EA4T steel in literature.

Data Availability

The data are available upon request by contacting with the corresponding author.

CRediT authorship contribution statement

Weiqian Chi: Methodology, Investigation, Writing – review & editing. **Wenjing Wang:** Methodology, Investigation, Writing – review & editing, Funding acquisition. **Ying Li:** Investigation, Writing – review & editing. **Wei Xu:** Investigation, Writing – review & editing. **Chengqi Sun:** Conceptualization, Methodology, Investigation, Writing – review & editing, Funding acquisition, Supervision.

Declaration of Competing Interest

The authors declare that they have no known competing financial interests or personal relationships that could have appeared to influence the work reported in this paper.

Acknowledgment

The authors acknowledge the support of the National Natural Science Foundation of China (91860112, 52075032) and Science and Technology Research and Development Program of China State Railway Group Co., Ltd. (P2020J024).

References

[1] T.D. Ngo, A. Kashani, G. Imbalzano, K.T.Q. Nguyen, D. Hui, Additive manufacturing (3D printing): A review of materials, methods, applications and challenges, Compos. Part B Eng. 143 (2018) 172–196.
[2] D. Zhang, D. Qiu, M.A. Gibson, Y. Zheng, H.L. Fraser, D.H. StJohn, M.A. Easton, Additive manufacturing of ultrafine-grained high-strength titanium alloys, Nature 576 (7785) (2019) 91–95.
[3] K. Markandan, R. Lim, P. Kumar Kanaujia, I. Seetoh, M.R. bin Mohd Rosdi, Z. H. Tey, J.S. Goh, Y.C. Lam, C. Lai, Additive manufacturing of composite materials and functionally graded structures using selective heat melting technique, J. Mater. Sci. Technol. 47 (2020) 243–252.
[4] L.E. Murr, S.A. Quinones, S.M. Gaytan, M.I. Lopez, A. Rodela, E.Y. Martinez, D. H. Hernandez, E. Martinez, F. Medina, R.B. Wicker, Microstructure and mechanical behavior of Ti–6Al–4V produced by rapid-layer manufacturing, for biomedical applications, J. Mech. Behav. Biomed. Mater. 2 (1) (2009) 20–32.
[5] G. Liu, X. Zhang, X. Chen, Y. He, L. Cheng, M. Huo, J. Yin, F. Hao, S. Chen, P. Wang, S. Yi, L. Wan, Z. Mao, Z. Chen, X.u. Wang, Z. Cao, J. Lu, Additive manufacturing of structural materials, Mater. Sci. Eng. R Rep. 145 (2021) 100596.
[6] A. Nouri, A. Rohani Shirvan, Y. Li, C. Wen, Additive manufacturing of metallic and polymeric load-bearing biomaterials using laser powder bed fusion: A review, J. Mater. Sci. Technol. 94 (2021) 196–215.
[7] A.A. Shanyavskiy, Very-High-Cycle-Fatigue of in-service air-engine blades, compressor and turbine, (Report), Sci. CHINA Physics, Mech. Astron. 57 (2014) 19.
[8] S. Jiao, C. Gao, L.i. Cheng, X. Li, Y.u. Feng, A very high-cycle fatigue test and fatigue properties of TC17 titanium alloy, J. Mater. Eng. Perform. 25 (3) (2016) 1085–1093.
[9] H.Q. Liu, C. He, Z.Y. Huang, Q.Y. Wang, Very high cycle fatigue failure mechanism of TC17 alloy, Acta Metall. Sin. 53 (2017) 1047–1054.
[10] S.V. Sajadifar, T. Wegener, G.G. Yapici, T. Niendorf, Effect of grain size on the very high cycle fatigue behavior and notch sensitivity of titanium, Theor. Appl. Fract. Mech. 104 (2019), 102362.
[11] Z.Y. Huang, H.Q. Liu, C. Wang, Q.Y. Wang, Fatigue life dispersion and thermal dissipation investigations for titanium alloy TC17 in very high cycle regime, Fatigue Fract. Eng. Mater. Struct. 38 (2015) 1285–1293.
[12] E. Wycisk, S. Siddique, D. Herzog, F. Walther, C. Emmelmann, Fatigue performance of laser additive manufactured Ti–6Al–4V in very high cycle fatigue regime up to 109 cycles, Front. Mater. 2 (2015).
[13] A. Tridello, J. Fiocchi, C.A. Biffi, G. Chiandussi, M. Rossetto, A. Tuissi, D.S. Paolino, VHCF response of heat-treated SLM Ti6Al4V Gaussian specimens with large loaded volume, Procedia Struct. Integr. 18 (2019) 314–321.
[14] C. Sun, W. Chi, W. Wang, Y. Duan, Characteristic and mechanism of crack initiation and early growth of an additively manufactured Ti-6Al-4V in very high cycle fatigue regime, Int. J. Mech. Sci. 205 (2021) 106591.

[15] J. Günther, D. Krewerth, T. Lippmann, S. Leuders, T. Tröster, A. Weidner, H. Biermann, T. Niendorf, Fatigue life of additively manufactured Ti–6Al–4V in the very high cycle fatigue regime, Int. J. Fatigue 94 (2017) 236–245.
[16] G. Qian, Y. Li, D.S. Paolino, A. Tridello, F. Berto, Y. Hong, Very-high-cycle fatigue behavior of Ti-6Al-4V manufactured by selective laser melting: Effect of build orientation, Int. J. Fatigue 136 (2020) 105628.
[17] W. Chi, G. Li, W. Wang, C. Sun, Interior initiation and early growth of very high cycle fatigue crack in an additively manufactured Ti-alloy, International Journal of Fatigue 160 (2022) 106862.
[18] Q. Song, C. Sun, Mechanism of crack initiation and early growth of high strength steels in very high cycle fatigue regime, Mater. Sci. Eng. A. 771 (2020), 138648.
[19] C. Sun, Q. Song, L. Zhou, X. Pan, Characteristic of interior crack initiation and early growth for high cycle and very high cycle fatigue of a martensitic stainless steel, Mater. Sci. Eng. A. 758 (2019) 112–120.
[20] T. Sakai, Y. Sato, N. Oguma, Characteristic S-N properties of high-carbon–chromium-bearing steel under axial loading in long-life fatigue, Fatigue Fract. Eng. Mater. Struct. 25 (2002) 765–773.
[21] A. Zhao, J. Xie, C. Sun, Z. Lei, Y. Hong, Prediction of threshold value for FGA formation, Mater. Sci. Eng. A. 528 (22-23) (2011) 6872–6877.
[22] C. Sun, X. Liu, Y. Hong, A two-parameter model to predict fatigue life of high-strength steels in a very high cycle fatigue regime, Acta Mech. Sin. 31 (3) (2015) 383–391.
[23] S. Leuders, M. Thöne, A. Riemer, T. Niendorf, T. Tröster, H.A. Richard, H.J. Maier, On the mechanical behaviour of titanium alloy TiAl6V4 manufactured by selective laser melting: Fatigue resistance and crack growth performance, Int. J. Fatigue 48 (2013) 300–307.
[24] L. Du, G. Qian, L. Zheng, Y. Hong, Influence of processing parameters of selective laser melting on high-cycle and very-high-cycle fatigue behaviour of Ti-6Al-4V, Fatigue Fract. Eng. Mater. Struct. 44 (1) (2021) 240–256.
[25] N. Shamsaei, A. Yadollahi, L. Bian, S.M. Thompson, An overview of Direct Laser Deposition for additive manufacturing; Part II: Mechanical behavior, process parameter optimization and control, Addit. Manuf. 8 (2015) 12–35.
[26] S.M. Thompson, L. Bian, N. Shamsaei, A. Yadollahi, An overview of direct laser deposition for additive manufacturing; Part I: Transport phenomena, modeling and diagnostics, Addit. Manuf. 8 (2015) 36–62.
[27] P. Edwards, M. Ramulu, Fatigue performance evaluation of selective laser melted Ti–6Al–4V, Mater. Sci. Eng. A. 598 (2014) 327–337.
[28] H. Masuo, Y. Tanaka, S. Morokoshi, H. Yagura, T. Uchida, Y. Yamamoto, Y. Murakami, Effects of defects, surface roughness and HIP on fatigue strength of Ti-6Al-4V manufactured by additive manufacturing, Procedia Struct. Integr. 7 (2017) 19–26.
[29] D. Greitemeier, F. Palm, F. Syassen, T. Melz, Fatigue performance of additive manufactured TiAl6V4 using electron and laser beam melting, Int. J. Fatigue 94 (2017) 211–217.
[30] S. Tammas-Williams, P.J. Withers, I. Todd, P.B. Prangnell, The influence of porosity on fatigue crack initiation in additively manufactured titanium components, Sci. Rep. 7 (2017) 7308.
[31] P. Li, D.H. Warner, J.W. Pegues, M.D. Roach, N. Shamsaei, N. Phan, Investigation of the mechanisms by which hot isostatic pressing improves the fatigue performance of powder bed fused Ti-6Al-4V, Int. J. Fatigue 120 (2019) 342–352.
[32] R. Molaei, A. Fatemi, N. Phan, Significance of hot isostatic pressing (HIP) on multiaxial deformation and fatigue behaviors of additive manufactured Ti-6Al-4V including build orientation and surface roughness effects, Int. J. Fatigue 117 (2018) 352–370.
[33] X. Shui, K. Yamanaka, M. Mori, Y. Nagata, K. Kurita, A. Chiba, Effects of post-processing on cyclic fatigue response of a titanium alloy additively manufactured by electron beam melting, Mater. Sci. Eng. A. 680 (2017) 239–248.
[34] M.C. Ding, Y.L. Zhang, H.T. Lu, Fatigue life prediction of TC17 titanium alloy based on micro scratch, Int. J. Fatigue 139 (2020), 105793.
[35] R.O. Ritchie, B.L. Boyce, J.P. Campbell, O. Roder, A.W. Thompson, W.W. Milligan, Thresholds for high-cycle fatigue in a turbine engine Ti–6Al–4V alloy, Int. J. Fatigue 21 (1999) 653–662.
[36] W. Chi, W. Wang, W. Xu, G. Li, X. Chen, C. Sun, Effects of defects on fatigue behavior of TC17 titanium alloy for compressor blades: Crack initiation and modeling of fatigue strength, Eng. Fract. Mech. 259 (2022), 108136.
[37] C. Bathias, P.C. Paris, Gigacycle fatigue in mechanical practice, CRC Press, New York, USA, 2004.
[38] Y. Murakami, Metal fatigue: effects of small defects and nonmetallic inclusions, Academic Press, Oxford, UK, 2019.
[39] C. Sun, Q. Song, A method for predicting the effects of specimen geometry and loading condition on fatigue strength, Metals 8 (2018) 811.
[40] H. Su, X. Liu, C. Sun, Y. Hong, Nanograin layer formation at crack initiation region for very-high-cycle fatigue of a Ti–6Al–4V alloy, Fatigue Fract. Eng. Mater. Struct. 40 (6) (2017) 979–993.
[41] Kevinsanny, S. Okazaki, O. Takakuwa, Y. Ogawa, K. Okita, Y. Funakoshi, J. Yamabe, S. Matsuoka, H. Matsunaga, Matsunaga, Effect of defects on the fatigue limit of Ni-based superalloy 718 with different grain sizes, Fatigue Fract. Eng. Mater. Struct. 42 (5) (2019) 1203–1213.
[42] X. Zhao, S. Wu, J. Bao, N. Ao, W. Peng, W. Sun, Experimental characterization and numerical modeling on the external impacting of high-speed railway axle EA4T steel, Eng. Fail. Anal. 125 (2021), 105449.
[43] J. Wang, Y. Zhang, Q. Sun, S. Liu, B. Shi, H. Lu, Giga-fatigue life prediction of FV520B-I with surface roughness, Mater. Des. 89 (2016) 1028–1034.
[44] W. Jinlong, P. Wenjie, Y.u. Jing, W. Jingsi, D. Mingchao, Z. Yuanliang, Effect of surface roughness on the fatigue failure and evaluation of TC17 titanium alloy, Mater. Sci. Technol. 37 (3) (2021) 301–313.
[45] P. Li, D.H. Warner, A. Fatemi, N. Phan, Critical assessment of the fatigue performance of additively manufactured Ti–6Al–4V and perspective for future research, Int. J. Fatigue 85 (2016) 130–143.
[46] H. Matsunaga, Y. Murakami, M. Kubota, J.H. Lee, Fatigue strength of Ti-6Al-4V alloys containing small artificial defects, Mater. Sci. Res. Int. 4 (2003) 263–269.
[47] J.W. Gao, X.N. Pan, J. Han, S.P. Zhu, D. Liao, Y.B. Li, G.Z. Dai, Influence of artificial defects on fatigue strength of induction hardened S38C axles, Int. J. Fatigue 139 (2020), 105746.
[48] Y.N. Hu, S.C. Wu, P.J. Withers, J. Zhang, H.Y.X. Bao, Y.N. Fu, G.Z. Kang, The effect of manufacturing defects on the fatigue life of selective laser melted Ti-6Al-4V structures, Mater. Des. 192 (2020), 108708.
[49] B.M. Schonbauer, H. Mayer, Effect of small defects on the fatigue strength of martensitic stainless steels, Int. J. Fatigue 127 (2019) 362–375.
[50] Y. Murakami, M. Endo, Effects of defects, inclusions and inhomogeneities on fatigue strength, Int. J. Fatigue 16 (3) (1994) 163–182.
[51] Q.Y. Wang, C. Bathias, N. Kawagoishi, Q. Chen, Effect of inclusion on subsurface crack initiation and gigacycle fatigue strength, Int. J. Fatigue 24 (2002) 1269–1274.
[52] C. Sun, Z. Lei, J. Xie, Y. Hong, Effects of inclusion size and stress ratio on fatigue strength for high-strength steels with fish-eye mode failure, Int. J. Fatigue 48 (2013) 19–27.
[53] J. Zhang, H. Li, B. Yang, B. Wu, S. Zhu, Fatigue properties and fatigue strength evaluation of railway axle steel: Effect of micro-shot peening and artificial defect, Int. J. Fatigue 132 (2020), 105379.
[54] B.M. Schönbauer, K. Yanase, M. Endo, The influence of various types of small defects on the fatigue limit of precipitation-hardened 17–4PH stainless steel, Theor. Appl. Fract. Mech. 87 (2017) 35–49.
[55] S. Hanaki, M. Yamashita, H. Uchida, M. Zako, On stochastic evaluation of S-N data based on fatigue strength distribution, Int. J. Fatigue 32 (3) (2010) 605–609.